Monthly Notices
of the
ROYAL ASTRONOMICAL SOCIETY

Mon. Not. R. Astron. Soc. **401,** 197–203 (2010) doi:10.1111/j.1365-2966.2009.15622.x

A quantitative determination of the AGN content in local ULIRGs through *L*-band spectroscopy

G. Risaliti,[1,2]★ M. Imanishi[3] and E. Sani[4]

[1]*INAF - Osservatorio Astrofisico di Arcetri, L.go E. Fermi 5, 50125 Firenze, Italy*
[2]*Harvard-Smithsonian Center for Astrophysics, 60 Garden St., Cambridge, MA 02138, USA*
[3]*National Astronomical Observatory, 2-21-1 Osawa, Mitaka, Tokyo 181-8588, Japan*
[4]*Dipartimento di Astronomia, Università di Firenze, L.go E. Fermi 2, 50125 Firenze, Italy*

Accepted 2009 August 26. Received 2009 August 26; in original form 2009 March 30

ABSTRACT

We present a quantitative estimate of the relative active galactic nucleus (AGN)/starburst content in a sample of 59 nearby ($z < 0.15$) infrared bright ultraluminous infrared galaxies (ULIRGs) taken from the 1-Jy sample, based on infrared *L*-band (3–4 μm) spectra. By using diagnostic diagrams and a simple deconvolution model, we show that at least 60 per cent of local ULIRGs contain an active nucleus, but the AGN contribution to the bolometric luminosity is relevant only in ∼15–20 per cent of the sources. Overall, ULIRGs appear to be powered by the starburst process, responsible for >85 per cent of the observed infrared luminosity. The subsample of sources optically classified as low-ionization nuclear emission-line regions (LINERs; 31 objects) shows a similar AGN/starburst distribution as the whole sample, indicating a composite nature for this class of objects. We also show that a few ULIRGs, optically classified as starbursts, have *L*-band spectral features suggesting the presence of a buried AGN.

Key words: galaxies: active – galaxies: starburst – infrared: galaxies.

1 INTRODUCTION

Ultraluminous infrared galaxies (ULIRGs, $L_{\rm IR} \sim L_{\rm BOL} > 10^{12}\,{\rm L}_{\odot}$) have been studied at all wavelengths, from radio to hard X-rays, with the primary aim of estimating the relative contribution of accretion and star formation activity to the bolometric luminosity.

Recently, *L*-band (3–4 μm) spectroscopy provided new powerful tools to perform this study. Imanishi & Dudley (2000), Risaliti et al. (2003), Imanishi, Dudley & Maloney (2006, hereafter I06), Risaliti et al. (2006a, hereafter R06), Imanishi et al. (2008) and Sani et al. (2008) analysed nearby bright ULIRGs from the *IRAS* Bright Galaxy Sample (Sanders et al. 2003) and the *IRAS* 1-Jy sample (Kim & Sanders 1998) and demonstrated that the active galactic nucleus (AGN) and starburst (SB) components can be disentangled in *L*-band spectra, using several indicators.

– 3.3 μm emission feature: this emission is due to polycyclic aromatic hydrocarbon (PAH) molecules, and is prominent in SB-dominated sources (equivalent width EW ∼ 110 nm), while it is weak or absent in AGN-dominated sources. This observational result is motivated by the different intrinsic emission of AGNs and SBs: the intense X-ray radiation of the former is believed to destroy the PAH molecules, which can instead survive in the SB radiation field.

– 3.4 μm absorption feature: in ULIRGs, the presence of this feature with an optical depth $\tau_{3.4} > 0.2$ is observationally associated to heavily obscured AGNs. This is due to the centrally concentrated emission of AGNs, which can be effectively covered by large columns of dust. Imanishi & Maloney (2003) demonstrated that a large-scale source, such as a SB, interspersed within the dust responsible for absorption, cannot have a 3.4 μm absorption feature with $\tau > 0.2$.

– Continuum slope: ULIRGs containing heavily obscured AGNs show a much redder *L*-band continuum than unobscured AGNs and SBs. This is due to the reddening effect of the covering dust. If the continuum is modelled with a simple power law in the λ–f_λ plane, i.e. $f_\lambda \propto \lambda^{\Gamma}$, the typical values for the slope Γ are $\Gamma \sim -0.5$ for unobscured AGNs and pure SB, while $\Gamma > 1$ for heavily obscured AGNs (R06).

– Bolometric ratios: the intrinsic ratio between the 3 μm and bolometric luminosity is ∼100 times higher in pure AGNs than in SBs (R06). The measured ratio in ULIRGs is therefore in itself an indicator of the possible presence of an AGN component.

The power of *L*-band spectroscopic analysis lays in the capability of detecting heavily obscured AGNs, which are missed at other wavelengths. The combination of the properties listed above implies that an AGN with an *L*-band optical depth $A_L \sim$ 1–5

★E-mail: risaliti@arcetri.astro.it

[corresponding to $A_V \sim 20$–100, i.e. completely absorbed from the ultraviolet (UV) to the near-infrared (IR)] can still be detectable in the *L*-band spectrum of ULIRGs, even when its contribution to the bolometric luminosity is negligible.

A quantitative application of the above diagnostics has been proposed by R06, who assumed that the *L*-band spectra can be reproduced as the combination of a fixed SB template and an AGN template with variable dust absorption. As a consequence, the model has two free parameters: the fraction of the AGN contribution to the *L*-band luminosity, α, and the optical depth τ_L of the dust absorbing the AGN component. These two parameters can be estimated from the observed continuum slope, Γ, and the equivalent width $EW_{3.3}$ of the 3.3 μm PAH emission feature.

In this paper we present the application of this method to a complete sample of 59 ULIRG with available *L*-band spectroscopic observations. The sample consists of all the ULIRGs in the *IRAS* 1-Jy sample with redshift $z < 0.15$. The optical classification (Veilleux, Kim & Sanders 1999) is AGN for 14 sources (25 per cent), SB for 12 sources (22 per cent) and low-ionization nuclear emission-line region (LINER) for 31 sources (56 per cent). Two sources are not optically classified. Our work is mostly based on published data, which already provided an AGN/SB classification, based on the diagnostic features summarized above. The significant improvement presented here consists in moving from a simple ULIRGs classification as SB or AGN, to a quantitative estimate of the contribution of the two components to the bolometric luminosity.

A similar approach has also been successfully used by Nardini et al. (2008) on *Spitzer*/Infrared Spectrograph (IRS) 5–8 μm spectra of a sample of local ULIRGs largely overlapping with the one presented here. We will discuss our results in comparison with those of Nardini et al. (2008) in Section 3.

2 DATA ANALYSIS

The observations in the Northern hemisphere have been performed with the Subaru (45 sources) and Infrared Telescope Facility (IRTF; six sources) telescopes, and have been presented in I06. In the Southern hemisphere the observations were made with the Very Large Telescope (VLT; eight sources). Four of these sources have been presented by R06 and Risaliti et al. (2006b), while the remaining four were observed in early 2006 with Infrared Spectrometer and Array Camera (ISAAC), with the same configuration as for the first eight sources, and reduced following the steps described in R06. We refer to R06 and I06 for a detailed description of the data reduction and a visual analysis of the spectra.

We performed a homogeneous analysis of all the sources in our sample, fitting each f_λ spectrum with a standard χ^2 minimization using stated observational uncertainties. The adopted model consists of a power-law continuum, and a Gaussian emission feature at rest-frame wavelength of 3.3 μm. For each source, the spectral interval used for the fit is $\lambda = 3.25(1+z) - 4.1$ μm, i.e. the region containing the 3.3 μm emission feature and the continuum at longer wavelengths up to the end of the *L* band. We excluded the wavelengths shortward of the PAH emission feature to avoid regions of bad atmospheric transmission, and possible distortions of the continuum slope due to ice absorption features (see R06 and I06 for more details). In a few spectra a hydrocarbon absorption feature at rest-frame wavelength $\lambda_{rest} = 3.4$–3.5 μm is clearly present. In these cases we added a Gaussian absorption component in our fits. In all the other cases we checked that this extra component is not required statistically. In Fig. 1 we show a few examples of the data and spectral fitting for representative objects in our sample.

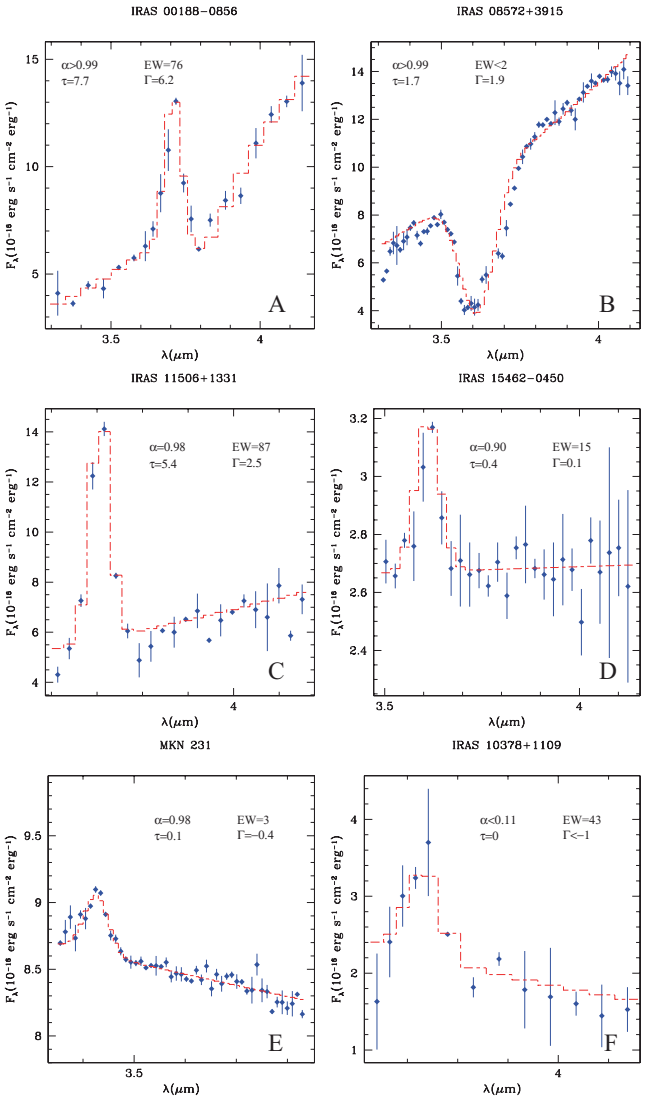

Figure 1. Six examples of our data and best-fitting models, including objects among the highest (B) and lowest (F) S/N. (A, B and C): sources *intrinsically* dominated by a heavily obscured AGN. The SB component is however strong in the *observed* spectra in (A) and (C). Note that (C) is optically classified as SB. (D and E): objects containing a weakly obscured AGN, which is dominant in the *L* band, but not in the Bolometric luminosity (see Table 1). (F): SB-dominated object.

In Table 1 we list the best-fitting parameters Γ and $EW_{3.3}$ for each source. A third important parameter which can be directly inferred from the analysis is the ratio between the luminosity in the *L* band and the bolometric one, obtained from *IRAS* fluxes. As shown in R06, these three parameters are enough to provide a classification of the sources with respect to their AGN/SB content. This is illustrated in Figs 2 and 3. In Fig. 2 we show the position of our sources in the Γ–$EW_{3.3}$ plane. We also show the regions occupied by obscured AGN, unobscured AGN and SBs, based on the calibration done in R06. Fig. 3 shows the measured *L* band to bolometric flux ratio, $R_L = \lambda f_\lambda(3.3\ \mu m)/F(8\text{–}1000\ \mu m)$ versus $EW_{3.3}$. We note that R_L is in principle a rather powerful indicator, given the huge difference between the *L* band to bolometric ratios for pure AGNs and pure SBs (of a factor of about 100; R06). However, it is not capable of giving an absolute estimate of the relative contributions of the AGN/SB components, because of the degeneracy introduced by

Table 1. Results from AGN-SB decomposition as described in the text. The horizontal lines divide the sources in groups according to their optical classification: LINERs (first group), SBs (second group), AGN (third group) and unclassified (the last two sources). The error on $\alpha_{\rm BOL}$ does not take into account the uncertainties on the *L* band to bolometric ratios. A more realistic estimate can be estimate from the scatter in Fig. 5 (see text for more details).

Source (instrument[a])	Γ	EW	τ	α_L	$\alpha_{\rm BOL}$	$\tau_{3.4}$	Cl(L)[b]	Cl(Sp)[c]
IRAS 00188−0856 (S)	6.2 ± 0.1	76 ± 13	7.7 ± 1.4	0.995 ± 0.003	0.91 ± 0.06	0.36 ± 0.06	AGN*	AGN
IRAS 02411+0353E (V)	-2.4 ± 2.2	177 ± 51	0[e]	<0.1[e]	$<10^{-3}$[e]	0[f]	–	SB
IRAS 02411+0353W (V)	-2.5 ± 3.0	183 ± 80	<3	<0.96	<0.18	0[f]	–	SB
IRAS 03250+1606 (S)	-1.8 ± 1.1	83 ± 22	0[d]	<0.52	<0.01	0[f]	AGN*	SB
IRAS 04103−2838 (V)	-0.1 ± 0.2	59 ± 6	0.7 ± 0.4	0.63 ± 0.07	0.02 ± 0.005	0[f]	–	AGN*
IRAS 08572+3915 (I)	1.9 ± 0.1	1 ± 1	1.7 ± 0.1	>0.99	>0.71	0.88 ± 0.05	AGN	AGN
IRAS 09039+0503 (S)	0.3 ± 0.8	257 ± 88	0[e]	<0.1[e]	$<10^{-3}$[e]	0[f]	AGN*	AGN*
IRAS 09116+0334 (S)	-1.9 ± 0.3	77 ± 18	0[d]	0.3 ± 0.2	$0.02^{+0.015}_{-0.015}$	0[f]	AGN*	SB
IRAS 09539+0857 (S)	-0.5 ± 0.2	101 ± 21	<0.2	<0.09	<0.01	0[f]	SB	AGN*
IRAS 10378+1108 (S)	-2.8 ± 1.2	43 ± 24	0[d]	0.6 ± 0.2	$0.02^{+0.02}_{-0.01}$	0[f]	SB	AGN*
IRAS 10485−1447 (S)	3.4 ± 0.2	41 ± 3	3.6 ± 0.3	0.98 ± 0.01	0.37 ± 0.03	0.25 ± 0.08	AGN*	AGN*
IRAS 10494+4424 (S)	-0.5 ± 0.2	126 ± 15	<0.2	<0.11	<0.01	0[f]	AGN*	SB
IRAS 11095−0238 (S)	1.5 ± 0.1	127 ± 26	5.7 ± 3.9	>0.95	>0.20	0[f]	SB	AGN
IRAS 12112+0305NE (V)	0.1 ± 1.0	69 ± 30	<3	0.63 ± 0.35	<0.04	0[f]	SB	SB
IRAS 12112+0305SW (V)	-0.9 ± 0.7	<300	–	–	–	0[f]	–	–
IRAS 12359−0725 (S)	2.3 ± 0.3	83 ± 17	4.6 ± 1.8	0.97 ± 0.02	0.25 ± 0.15	0[f]	AGN*	AGN*
IRAS 12127−1412 (S)	2.1 ± 0.1	21 ± 6	2.0 ± 0.1	0.97 ± 0.01	0.25 ± 0.06	0[f]	AGN	AGN
IRAS 13335−2612 (V)	2.0 ± 1.5	220 ± 146	0[e]	<0.1[e]	$<10^{-3}$[e]	0[f]	–	SB
IRAS 14252−1550E (S)	0.1 ± 1.6	85 ± 32	–	–	–	0[f]	–	–
IRAS 14252−1550W (S)	0.1 ± 0.3	91 ± 20	<1.8	0.55 ± 0.30	0.01 ± 0.008	0[f]	AGN*	SB
IRAS 14348−1447 (V)	0.4 ± 0.4	110 ± 30	1.2 ± 1.1	<0.72	<0.03	0[f]	AGN*	AGN*
Arp 220 (I)	0.4 ± 0.2	79 ± 9	1.8 ± 0.7	0.69 ± 0.10	0.02 ± 0.01	0[f]	SB	AGN*
IRAS 16090−0139 (S)	2.5 ± 5.8	<180	–	–	–	0[f]	AGN*	AGN*
IRAS 16468+5200 (S)	-2.8 ± 1.6	184 ± 70	–	<0.54	<0.01	0[f]	SB	AGN*
IRAS 16487+5447 (S)	-2.0 ± 1.4	126 ± 37	–	–	–	0[f]	AGN*	SB
IRAS 17028+5817 (S)	-2.1 ± 0.2	83 ± 11	0[d]	0.24 ± 0.10	0.003 ± 0.001	0[f]	AGN*	SB
IRAS 17044+6720 (S)	1.3 ± 0.1	18 ± 4	1.4 ± 0.1	0.95 ± 0.01	0.17 ± 0.03	0.14 ± 0.09	AGN	AGN
IRAS 21219−1757 (S)	-0.7 ± 0.1	1 ± 0.5	0[d]	0.99 ± 0.005	0.47 ± 0.10	0[f]	–	–
IRAS 21329−2346 (S)	-0.4 ± 0.7	79 ± 16	<1.5	<0.74	<0.02	0[f]	AGN*	AGN*
IRAS 23234+0946 (S)	0.6 ± 0.1	146 ± 14	0[e]	<0.1[e]	$<10^{-3}$[e]	0[f]	SB	SB
IRAS 23327+2913 (S)	0.1 ± 0.8	52 ± 16	<2.0	0.70 ± 0.20	0.023 ± 0.017	0[f]	SB	AGN*
IRAS 10190+1322E(S)	-0.5 ± 0.1	82 ± 3	<0.2	0.26 ± 0.06	0.003 ± 0.001	0[f]	SB	SB
IRAS 10190+1322W(S)	-2.2 ± 0.4	79 ± 20	0[d]	<0.46	<0.02	0[f]	SB	SB
IRAS 11387+4116 (S)	-1.1 ± 0.4	106 ± 31	0[d]	<0.45	<0.02	0[f]	SB	SB
IRAS 11506+1331 (S)	2.5 ± 0.2	87 ± 10	5.4 ± 1.3	0.98 ± 0.01	0.35 ± 0.12	0[f]	AGN	AGN
IRAS 13509+0442 (S)	0.2 ± 1.3	157 ± 35	<3.4	<0.97	<0.28	0[f]	SB	SB
IRAS 13539+2920 (S)	-0.6 ± 0.6	94 ± 20	<2.8	<0.73	<0.03	0[f]	SB	SB
IRAS 14060+2919 (S)	-0.2 ± 0.2	185 ± 15	0[e]	<0.1[e]	$<10^{-3}$[e]	0[f]	SB	SB
IRAS 15206+3342 (S)	0.2 ± 0.2	71 ± 14	1.1 ± 0.8	0.64 ± 0.15	0.02 ± 0.01	0[f]	SB	SB
IRAS 15225+2350 (S)	1.3 ± 0.6	28 ± 13	1.5 ± 0.8	0.93 ± 0.04	0.12 ± 0.07	0[f]	AGN*	AGN*
IRAS 16474+3430 (S)	0.5 ± 0.4	103 ± 29	4.8 ± 13.4	0.90 ± 0.48	0.08 ± 0.36	0[f]	AGN*	SB
IRAS 20414−1651 (S)	-1.4 ± 1.0	77 ± 18	1.5 ± 3.4	<0.66	<0.02	0[f]	SB	SB
IRAS 21208−0519 (S)	-0.4 ± 3.1	169 ± 102	–	–	–	0[f]	SB	SB
IRAS 05189−2524 (V)	0.1 ± 0.1	7 ± 1	0.4 ± 0.1	0.96 ± 0.01	0.18 ± 0.01	0[f]	AGN	AGN
IRAS 08559+1053 (S)	-0.2 ± 0.1	13 ± 4	0.3 ± 0.1	0.91 ± 0.03	0.09 ± 0.03	0[f]	AGN	–
IRAS 12072−0444 (S)	1.2 ± 0.2	86 ± 19	3.5 ± 1.9	0.90 ± 0.08	0.08 ± 0.06	0.57 ± 0.11	AGN	–
Mrk 273 (I)	0.1 ± 0.1	31 ± 5	0.5 ± 0.2	0.81 ± 0.04	0.04 ± 0.01	0[f]	AGN	AGN
IRAS 13443+0802 (S)	-0.6 ± 1.1	111 ± 56	<2.0	<0.5	<0.01	0[f]	SB	–
PKS 1345+12 (I)	0.7 ± 0.1	7 ± 3	0.9 ± 0.1	0.97 ± 0.01	0.25 ± 0.08	0[f]	AGN	AGN
IRAS 15130−1958 (S)	0.2 ± 0.1	8 ± 1	0.5 ± 0.1	0.95 ± 0.01	0.17 ± 0.05	0[f]	AGN	–
IRAS 17179+5444 (S)	1.3 ± 0.3	24 ± 13	1.5 ± 0.4	0.94 ± 0.04	0.14 ± 0.09	1 ± 0.5	AGN	–
Mrk 1014 (I)	-0.7 ± 0.1	8 ± 1	0[d]	0.91 ± 0.01	0.09 ± 0.01	0[f]	AGN	–
IRAS 07599+6508 (S)	-0.3 ± 0.1	1 ± 1	0.2 ± 0.05	>0.99	>0.7	0[f]	AGN	–
IRAS 11598−0112 (S)	-0.3 ± 0.2	5 ± 3	0.1 ± 0.1	0.96 ± 0.03	0.19 ± 0.10	0[f]	AGN	–
Mrk 231 (I)	-0.4 ± 0.1	3 ± 0.5	0.1 ± 0.05	0.98 ± 0.01	0.28 ± 0.02	0[f]	AGN	AGN
IRAS 15462−0450 (S)	0.1 ± 0.2	15 ± 5	0.4 ± 0.2	0.90 ± 0.04	0.09 ± 0.03	0[f]	AGN	–
IRAS 12127−1412 (S)	2.0 ± 0.1	21 ± 6	2.0 ± 0.1	0.97 ± 0.01	0.25 ± 0.06	0.25 ± 0.07	AGN	AGN

Table 1 – *continued*

Source (instrument[a])	Γ	EW	τ	α_L	α_{BOL}	$\tau_{3.4}$	Cl(L)[b]	Cl(Sp)[c]
IRAS 14197+0813 (S)	-0.6 ± 0.5	130 ± 16	<0.9	<0.67	<0.02	0[f]	–	–
IRAS 14485−2434 (S)	0.7 ± 0.1	65 ± 8	1.7 ± 0.3	0.80 ± 0.04	0.04 ± 0.01	0[f]	AGN	–

[a]Telescope/instrument of the observation: S: Subaru; V: VLT-ISAAC; I: IRTF.
[b]Classification from 'standard' *L*-band diagnostics (from I06), based on the PAH EW and the presence of absorption features. An asterisk indicates a weak evidence for the presence of the AGN.
[c]Classification based on *Spitzer*/IRS spectroscopy (from Imanishi et al. 2007).
[d]Absorption is assumed to be $\tau = 0$, due to the steep continuum ($\Gamma < -0.5$ at >90 per cent confidence level).
[e]Values and upper limits obtained assuming the source is pure SB, due to the high equivalent width of the 3.3 μm feature (EW > 110 nm at >90 per cent confidence level).
[f]3.4 μm absorption not required to adequately fit the spectrum.

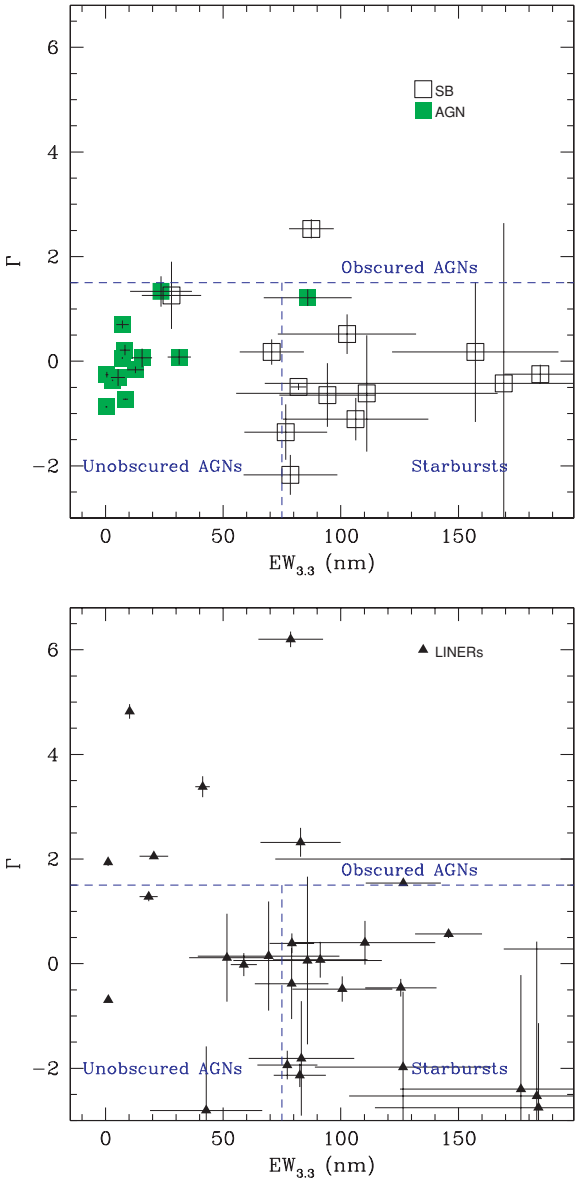

Figure 2. 3–4 μm continuum slope (in a $\lambda - f_\lambda$ spectrum) versus equivalent width of the 3.3 μm PAH emission feature for the sample of $z < 0.15$ ULIRGs in the 1-Jy sample (Veilleux et al. 1999). The dashed lines mark the SB, unobscured AGN and AGN zones according to the results of Risaliti et al. (2006a). The sample is split into two different panels for clarity, depending of the optical classification of the objects, marked as different symbols.

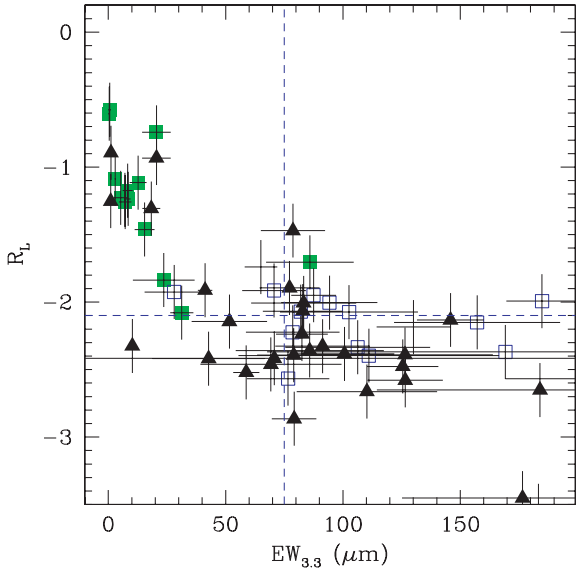

Figure 3. Ratio between *L* band and bolometric luminosity, R_L, versus equivalent width of the 3.3 μm PAH emission feature. We adopt 20 per cent errors on R_L, estimated from the average *IRAS* and *L*-band absolute calibration uncertainties. The dashed lines mark the SB and AGN zones according to R06. Symbols are the same as in Fig. 2.

the extinction of the AGN component: the same ratio can be obtained with a faint, unobscured AGN mixed with a powerful SB, or with a much more luminous, even bolometrically dominant, but heavily obscured AGN. However, on average we observe an anticorrelation between this AGN indicator and the 3.3 μm PAH SB indicator (Fig. 3).

The second part of our analysis consists of a quantitative estimate of the physically relevant parameters for our sources, i.e. the absorption of the AGN component, τ, and the continuum fraction of emission due to the AGN, α (estimated at 3.3 μm). We use the simple method described in R06: the total spectrum is reproduced as a combination of an AGN power-law component, $f_{AGN} = C_1 \lambda^{\Gamma}_{AGN}$, absorbed by dust following the extinction law $\tau \propto \lambda^{-1.75}$ (Cardelli, Clayton & Mathis 1989), and a SB component, consisting of a power-law continuum $f_{SB} = C_2 \lambda^{\Gamma}_{SB}$ and a Gaussian emission line at $\lambda = 3.3$ μm with a fixed equivalent width EW_{SB} with respect to the SB continuum component. Following the results obtained for bright ULIRGs in R06, we chose the values $\Gamma_{AGN} = -0.5$, $\Gamma_{SB} = -0.5$ and $EW_{SB} = 110$ nm for the AGN and SB templates.

Using this model, with simple algebra we can obtain the observed parameters Γ and $EW_{3.3}$ as a function of the extinction τ and the AGN fraction $\alpha = C_1/(C_1 + C_2)$. τ and α can then be obtained

simply inverting these equations, as shown in R06. The final result is

$$\tau_L = \frac{\mathrm{EW_{SB}}\Gamma - \mathrm{EW_{3.3}}}{\beta(\mathrm{EW_{SB}} - \mathrm{EW_{3.3}})}, \quad (1)$$

$$\alpha = \frac{\mathrm{EW_{SB}} - \mathrm{EW_{3.3}}}{(\mathrm{EW_{SB}} - \mathrm{EW_{3.3}}) + \mathrm{EW_{3.3}}\,\mathrm{e}^{-\tau_L}}, \quad (2)$$

where β is the index of the extinction power law ($\beta = 1.75$). The errors on α and τ can be directly estimated from the above equations, as shown in the appendix of R06.

In five cases the errors on the observed parameters are too high to obtain significant estimates of τ and α. For all the other sources the results are listed in Table 1.

The application of this model to the measured parameters listed in Table 1 is not straightforward for all sources: in several cases the best-fitting values and the 90 per cent confidence intervals of one or both of $\mathrm{EW_{3.3}}$ and Γ are outside the 'allowed range' of our model, $\Gamma < \Gamma_{\rm min} = -0.5$ and $\mathrm{EW_{3.3}} > \mathrm{EW_{max}} = 110$ nm. In these cases our approach is the following.

(i) If $\Gamma < -0.5$ at >90 per cent statistical significance, we assume $\tau = 0$ and we estimate the relative AGN fraction using $\mathrm{EW_{3.3}}$: $\alpha = 1 - \mathrm{EW_{3.3}}/(110\,\mathrm{nm})$.

(ii) If $\mathrm{EW_{3.3}} > 110$ nm and Γ is not higher than the pure SB value $\Gamma_{\rm SB} = \Gamma_{\rm min} = -0.5$, we assume the source is predominantly powered by a pure SB and we put an upper limit of 1 per cent to the AGN contribution. We note that in no case $\mathrm{EW_{3.3}} > 110$ nm and $\Gamma > -0.5$ at a 90 per cent confidence level. The values of α and τ so obtained are shown in Table 1.

The final step in our analysis is the estimate of the fraction of the bolometric emission due to the AGN, $\alpha_{\rm BOL}$. This quantity is related to the AGN fraction in the L band, α, through two new parameters, i.e. the ratio between the L band and bolometric luminosities for pure AGN and pure SB, $R_{\rm AGN}$ and $R_{\rm SB}$. Simple calculations show that $\alpha_{\rm bol} = \alpha/[\alpha + K(1-\alpha)]$, where $K = R_{\rm AGN}/R_{\rm SB}$. Following the results obtained for bright sources (R06) we use $R_{\rm AGN} = 0.2$ and $R_{\rm SB} = 0.002$. The factor $K = 100$ in the above equation imply that the bolometric contribution of the AGN can be small even in those cases where the AGN component is dominant in the L band. The values of $\alpha_{\rm BOL}$ estimated using the above equation are listed in column 6 of Table 1. The uncertainties related to the factor K [$\log(K) \sim 2 \pm 0.5$; R06] are discussed in Section 3.3.

3 DISCUSSION

The application of our model to the 59 $z < 0.15$ ULIRGs in the 1-Jy sample of Veilleux et al. (1999) provided a quantitative estimate of the AGN/SB contribution in ULIRGs, and in particular in those optically classified as LINERs.

Here we (1) review and discuss our results, (2) compare them with the optical spectroscopic classification, and with the other multiwavelength AGN/SB indicators summarized in the Introduction and (3) discuss the uncertainties of our approach.

3.1 The AGN content in ULIRGs

The most relevant result of the present work is a quantitative estimate of the contributions of the two energy sources to the luminosity of ULIRGs. The estimated AGN fractions in the L band and in the total emission are summarized in the histograms in Fig. 4. The comparison between the two distributions shows the power

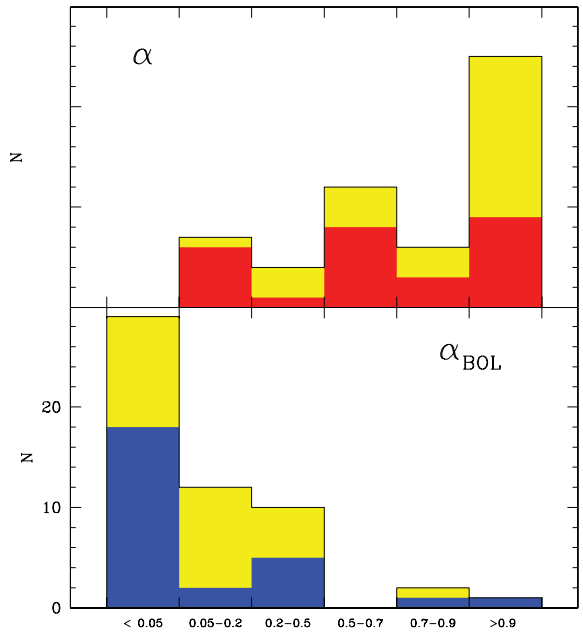

Figure 4. Distribution of the relative AGN contribution to the L-band emission (upper panel) and to the bolometric emission (lower panel) in our sample of ULIRGs. Blue and red (dark) histograms refer to LINERs only, while yellow (light) histograms refer to the whole sample.

of our diagnostics: the AGN, when present, dominates the L-band emission in most cases, even in objects where its contribution to the total luminosity is negligible. We note that our estimates strongly depend on the modelization of the SB/AGN emission. In particular, we assume a fixed SB template, with no free parameter. We expect this to be a simplification of a more complex spectral behaviour, in at least two respects: (a) the intrinsic equivalent width of the 3.3 μm emission feature (assumed to be $\mathrm{EW_{3.3}} = 110$ nm in our model) shows a significant spread among pure SBs, and (b) the observed SB emission could be affected by some reddening/absorption, as suggested by the large spread of the ratio between flux of the 3.3 μm feature and the bolometric emission in pure SBs (I06). Therefore, we believe our analysis provides correct results in a statistical sense for the whole sample, but can be affected by larger uncertainties than estimated in Table 1. We will discuss this issue in more detail in Section 3.3.

Overall, our analysis shows that the following.

– An AGN is present in most (>60 per cent) ULIRGs. This fraction drops to >30 per cent for LINERs (however, in several objects with low signal-to-noise ratio (S/N) the upper limit for the AGN fraction is quite high, see Table 1).

– The contribution of AGNs to the L-band emission is >50 per cent, while the fraction of the bolometric luminosity of ULIRGs due to AGNs is <20 per cent. Restricting to LINERs, the fraction of AGN contribution is <30 per cent in the L band, and <15 per cent bolometrically.

– In a few LINERs the presence of a heavily obscured AGN is bolometrically significant. On the other side there is an indication that most of the heavily obscured AGNs are LINERs (this is based only on ∼five–eight objects, so it needs to be confirmed with larger samples). This finding confirms the heterogeneous nature of this class of objects, which are on average dominated by SB emission, but can host powerful buried AGNs.

– In our model, quasi-stellar object (QSO) class luminous buried AGNs are found only in a small fraction of ULIRGs classified optically as LINERs or SBs.

3.2 Comparison with other AGN indicators

An AGN/SB classification for most of our sources has been presented, based on observations at other wavelength, or on a different analysis of *L*-band data.

Optical. Fig. 2 shows the classification of our sources in a continuum slope–PAH EW plot, for each optical class: AGN, SB and LINER. AGNs and SBs are clearly separated, and are located in the regions found by R06. Two exceptions are found among optically classified SBs: two sources, IRAS 20414−1651 and IRAS 11506+1331 (panel C in Fig. 1) show signatures of the presence of absorbed AGNs, which were missed by studies at other wavelengths. LINERs are spread throughout the plot, confirming their composite nature, as quantitatively shown in Table 1 and Fig. 4.

L-band absorption features. Aliphatic hydrocarbon absorption features at rest-frame wavelengths 3.4–3.5 μm have been detected in seven sources (three AGNs and four LINERs). All these objects have a clear detection of an AGN according to our model. Moreover, they are all associated to steep continua, with estimated continuum extinction $\tau > 1$ (see also Sani et al. 2008). Therefore, this correlation is a further independent confirmation of the validity of our diagnostics.

Previous L-band diagnostics. Most of the sources in our sample were presented and discussed in I06. In this work, the possible presence of the AGN in this work is estimated through the EW of the 3.3 μm PAH and the presence of absorption features. The final classification is shown in Table 1, and is in general agreement with our results. We stress again the two main improvements in the analysis presented here: a *quantitative* estimate of the relative AGN/SB contributions, and the inclusion of the continuum reddening as a further indicator of an obscured AGN (e.g. the source C in Fig. 1).

Mid-IR diagnostics. Imanishi et al. (2007) presented complete *Spitzer*/IRS spectroscopy of most of our sources, and an AGN/SB classification based on several diagnostic features (PAH emission at 6.2, 7.7 and 11.3 μm, silicate absorption at ∼9–10 μm). The results are shown in the last column of Table 1, and again are in good agreement with the conclusions presented here, with the same limitations discussed above for previous *L*-band diagnostics.

Nardini et al. (2008) performed an analysis of the same *Spitzer* spectra, focusing on the 5–8 μm spectral range, and applying an analysis similar to the one presented here. The results on the single sources are in excellent agreement in the two works: this can be verified comparing our estimates with their table 1. Here we only note that the *L*-band analysis, besides providing an independent AGN/SB deconvolution, has a higher diagnostic power, especially for ULIRGs hosting highly obscured AGNs, thanks to the higher contrast between AGN and SBs in the *L* band than at 5–8 μm.

Alternative, powerful mid-IR indicators of the AGN/SB contributions in ULIRGs are the silicate absorption features in the 9–10 μm band (Spoon et al. 2007), and the presence of high-ionization emission lines (Farrah et al. 2007). These studies, performed on samples with large overlaps with ours, provide results in good agreement with our classification. However, as for the other approaches described in this section, no quantitative estimates have been done based on these indicators.

X-rays. A strong X-ray emission is one of the strongest AGN indicators. If the obscuration of the AGN is not too high (column densities $N_{\rm H} < 10^{24}\,{\rm cm}^{-2}$), the primary AGN spectrum is directly visible at energies below 10 keV, providing a good estimate of its total luminosity, through bolometric corrections obtained from AGN spectral energy distributions (SEDs; e.g. Risaliti & Elvis 2004). If the obscuration is higher, only the reflection component is visible in the X-rays. In these cases, the spectral features of the reflection spectrum can identify the presence of the AGN, however, a good estimate of its total luminosity is not possible, due to the large uncertainty in the reflection efficiency. Extensive studies of local ULIRGs (e.g. Franceschini et al. 2003; Ptak et al. 2003) show that the current X-ray observatories can provide useful spectra for this diagnostics only for the 10–20 brightest sources, while most of the ULIRGs in our sample are too faint for this kind of analysis. The agreement between X-ray and *L*-band diagnostics for the few ULIRGs with high quality X-ray spectra is quite good (Sani et al. 2008; Braito et al. 2009). However, this analysis cannot be extended to more sources until more sensitive X-ray observatories are available.

3.3 Model uncertainties

The model presented here is based on a series of strong assumptions, which may introduce systematic errors, in addition to the statistical errors obtained from the fitting procedure. The main possible simplifications, already discussed in R06, are the assumption of fixed AGN and SB templates, and the absence of any absorption/reddening in the SB component. Other possible relevant effects may be caused by different dust extinction curves from the one assumed here.

Regarding possible obscuration of the SB component, we note that, though it cannot be excluded, it is not strongly required by the data. Physically, this may be due to the origin of the SB emission: the integrated contribution of a large number ($>10^6$) of single sources. Each single star can be heavily absorbed (as observed, for example, in the central regions of our own Galaxy), but the single differences are smeared out by the large number of sources, producing a rather constant spectral profile of the total emission. Regardless of the physical interpretation, this is also suggested by the observations: the highest quality spectra of pure SB are remarkably similar, both in the *L* band (R06) and in the 5–8 μm range (Brandl et al. 2006; Nardini et al. 2008).

Regarding the fixed AGN and SB templates, this is an obvious oversimplification, as shown by the scatter in the spectral parameters (Fig. 2; R06). We may try to estimate the effect of this scatter by changing the parameters of the pure AGN and pure SB templates, and reporting how this affects the estimate of the parameters α and τ. Since this scatter is hard to measure in a self-consistent way, we prefer to adopt a different, observation-based approach. In order to do this, we notice that our model can easily provide an estimate of the expected bolometric luminosity for each source, as a function of $R_{\rm AGN}$, $R_{\rm SB}$, the model parameters α and τ and the observed *L*-band luminosity, $L_{3-4}^{\rm OBS}$. In particular,

$$L_{\rm BOL} = [\alpha R_{\rm AGN} + (1-\alpha) R_{\rm SB}] L_{3-4}^{\rm INTR}, \quad (3)$$

where $L_{3-4}^{\rm INTR}$ is the intrinsic *L*-band luminosity (i.e. corrected for the extinction of the AGN component) and is related to the observed one by $L_{3-4}^{\rm INTR} = L_{3-4}^{\rm OBS}/[\alpha + (1-\alpha)\,{\rm e}^{-\tau}]$. Our estimate of $L_{\rm BOL}$ can then be compared with the observed $L_{\rm BOL}$, as measured by *IRAS*, by using the standard calibration of Sanders & Mirabel (1996). In Fig. 5 we plot two relations.

– In the upper panel the ratio $R_{\rm CORR}$ between the absorption-corrected *L*-band luminosity, $L_{3-4}^{\rm INTR}$, and the measured bolometric luminosity is plotted versus the *L*-band AGN fraction, α. The continuous line is the expected relation based on our model, with no

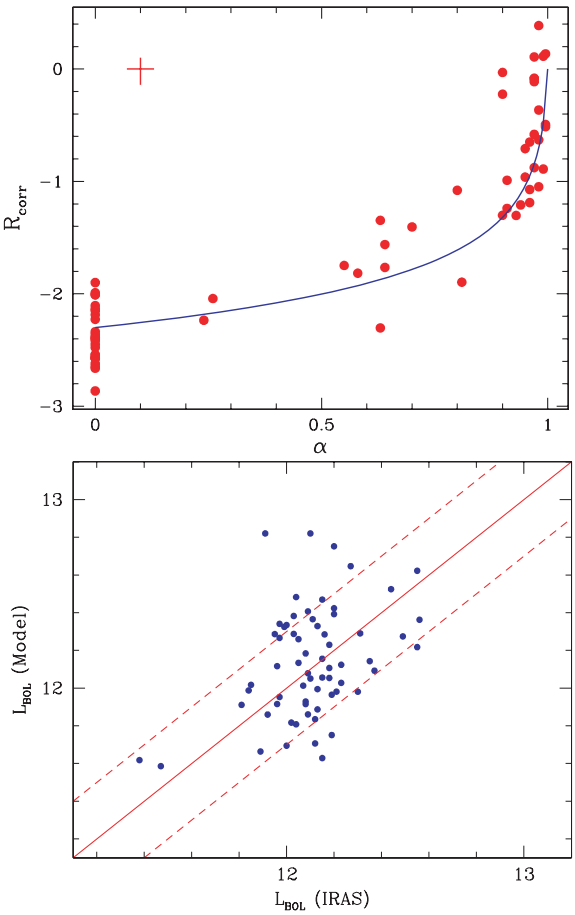

Figure 5. Top panel: ratio between intrinsic *L*-band and bolometric luminosity versus the AGN fraction α obtained from our analysis. The blue continuous line is that expected based on our model. The cross on the top left-hand corner indicates the average statistical errors on the two plotted quantities. Bottom panel: comparison between the estimated and measured bolometric luminosities. The 0.3 dex dispersion around the 1:1 relation is a fair estimate of the total uncertainty in our prediction of the AGN and SB bolometric contributions.

free parameters. In particular, the shape of the curve is determined by the mathematical relations between the model parameters, while the values at $\alpha = 0$ and 1 are the parameters R_{SB} and R_{AGN}, respectively. Overall, the agreement between the expected curve and the data is quite good. This is a strong confirmation of the validity of our method: our simple, two-parameter model can successfully predict the intrinsic *L* band to bolometric ratio.

– In the lower panel we directly compare the predicted and measured values of L_{BOL}. This is the most direct way to estimate the overall uncertainties in our analysis. These include both the statistical errors from the spectral fits, and the systematic errors due to the fixed templates. The dispersion from the 1:1 relation is lower than 0.3 dex. This is enough to provide a rough estimate of the AGN contribution in single sources, and an accurate average estimate for the whole sample.

4 CONCLUSIONS

L-band spectral analysis of ULIRGs is a powerful way to disentangle the AGN and SB contribution to the bolometric emission. This is primarily due to the diagnostic power of (a) the 3.3 μm PAH emission in SBs, (b) the continuum slope, indicative of the reddening of the AGN component, (c) the high ratio (about 100) between the AGN and SB emission at 3 μm, for the same bolometric luminosity.

We applied a simple model to the available *L*-band spectra of 59 ULIRGs from the 1-Jy sample, at redshift $z < 0.15$, in order to detect and quantitatively estimate the AGN contribution to the emission of these sources. We find that AGNs are present in 60 per cent of ULIRGs, but in most cases they are not the main energy source. As a consequence, their overall contribution to the total ULIRG luminosity is ∼20 per cent. We find that the subsample of objects optically classified as LINERs is rather composite, with similar AGN/SB fractions as the whole ULIRGs sample.

Our analysis revealed several objects optically classified as SB or LINERs, and/or with weak or absent previous evidence of the presence of an AGN in the near/mid-IR, which according to our model host a powerful, obscured AGN. We plan to observe these objects in the hard X-rays, in order to obtain an independent, unambiguous confirmation of these findings.

ACKNOWLEDGMENTS

We are grateful to the referee for his/her constructive comments which significantly helped to improve this paper. This work has been partially supported by contract ASI-INAF I/023/05/0.

REFERENCES

Brandl B. R. et al., 2006, ApJ, 653, 1129
Braito V., Reeves J. N., Della Ceca R., Ptak A., Risaliti G., Yaqoob T., 2009, A&A, 504, 53
Cardelli J. A., Clayton G. C., Mathis J. S., 1989, ApJ, 345, 245
Farrah D. et al., 2007, ApJ, 667, 149
Franceschini A. et al., 2003, MNRAS, 343, 1181
Imanishi M., Dudley C. C., 2000, ApJ, 545, 701
Imanishi M., Maloney P. R., 2003, ApJ, 588, 165
Imanishi M., Dudley C. C., Maloney P. R., 2006, ApJ, 637, 114 (I06)
Imanishi M., Dudley C. C., Maiolino R., Maloney P. R., Nakagawa T., Risaliti G., 2007, ApJS, 171, 72
Imanishi M., Nakagawa T., Ohyama Y., Shirahata M., Wada T., Onaka T., Oi N., 2008, PASJ, 60, 489
Kim D.-C., Sanders D. B., 1998, ApJS, 119, 41
Nardini E., Risaliti G., Salvati M., Sani E., Imanishi M., Marconi A., Maiolino R., 2008, MNRAS, 385, L130
Ptak A., Heckman T., Levenson N. A., Weaver K., Strickland D., 2003, ApJ, 592, 782
Risaliti G., Elvis M., 2004, in Barger A. J., ed., Astrophys. Space Sci. Library, Vol. 308, Supermassive Black Holes in the Distant Universe. Kluwer, Dordrecht, p. 187
Risaliti G. et al., 2003, ApJ, 595, L17
Risaliti G. et al., 2006a, MNRAS, 365, 303 (R06)
Risaliti G. et al., 2006b, ApJ, 637, L17
Sanders D. B., Mirabel I. F., 1996, ARA&A, 34, 749
Sanders D. B., Mazzarella J. M., Kim D.-C., Surace J. A., Soifer B. T., 2003, AJ, 126, 1607
Sani E. et al., 2008, ApJ, 675, 96
Spoon H. W. W., Marshall J. A., Houck J. R., Elitzur M., Hao L., Armus L., Brandl B. R., Charmandaris V., 2007, ApJ, 654, L49
Veilleux S., Kim D.-C., Sanders D. B., 1999, ApJS, 22, 113

This paper has been typeset from a TEX/LATEX file prepared by the author.